VIII International Conference on Fracture Mechanics of Concrete and Concrete Structures
FraMCoS-8
J.G.M. Van Mier, G. Ruiz, C. Andrade, R.C. Yu and X.X. Zhang (Eds)

DUAL-LATTICE-BASED SIMULATIONS OF COUPLED FRACTURE-FLOW IN REINFORCED CONCRETE

TOSHIHIDE SAKA*, JOHN E. BOLANDER† AND PETER GRASSL‡

* Kajima Technical Research Institute
Tobitakyu 2-19-1, Chofu-shi, Tokyo, 182-0036 Japan
e-mail: sakat@kajima.com

† University of California, Davis
One Shields Avenue, Davis, CA 95616, USA
e-mail: jebolander@ucdavis.edu

‡ University of Glasgow
Oakfield Avenue, Glasgow G128LT, United Kingdom
e-mail: peter.grassl@glasgow.ac.uk

Key words: Dual lattice, Coupled fracture-flow, Reinforced concrete, Mass transport, Water absorption, Cracking.

Abstract: Although reinforced concrete design typically allows for non-critical cracking of the concrete, such cracking is known to increase the effective permeability of concrete, which can promote various forms of structural deterioration. Numerical modeling offers opportunities for the study of these durability problems. In particular, lattice models are attractive for this purpose. The present work describes the fundamental concept and related recent developments of a dual-lattice model for coupled fracture-flow analyses of cementitious materials. The capabilities of this model are demonstrated by simulating water absorption in cracked reinforced concrete, the experiment of which was performed by Zhang et al. [24]. Comments are provided regarding more realistic simulations of reinforced concrete durability problems and potential future developments of this model.

1 INTRODUCTION

Design codes for structural concrete typically allow for non-critical cracking, and therefore cracking is inevitable in reinforced concrete structures. However, such cracking is known to accelerate the transport of moisture and other deleterious substances such as chlorides or sulphates, which greatly increases the potential for reinforcing steel corrosion and other mechanisms that lead to severe deterioration of reinforced concrete structures. Understanding such coupled fracture-flow phenomena is essential for the study of reinforced concrete durability.

Numerical modeling offers opportunities for the study of these durability problems, complementing what knowledge can be gained from physical testing. Due in part to the use of discrete, two-node elements, lattice models are simple and effective in simulating fracture of such quasi-brittle materials [1-4] . Furthermore, recent developments of the dual-lattice concept [5-7] offer opportunities for realistic simulations of flow through fractured concrete materials.

This paper first describes the fundamental concept of the dual-lattice models, in which the duality between the Delaunay tessellation and Voronoi diagram is utilized. Based on this

concept and use of the finite volume method, the discrete advection-diffusion equation on the flow lattice is derived and implemented. Secondly, the proposed method is verified by solving several basic problems. Finally, numerical simulations of water absorption in cracked reinforced concrete demonstrate the capabilities of the present method.

2 FORMULATION

2.1 Dual-lattice concept

Dual-lattice models, as shown in **Figure 1**, are constructed by the following procedure: 1) Prepare a set of arbitrary points in the computational domain; 2) Decompose the domain into a set of tetrahedra (in 3D) or triangles (in 2D) using the Delaunay tessellation [8]; 3) Take the Delaunay edges as elements of the structural lattice; 4) Decompose the domain into polyhedra (in 3D) or polygons (in 2D) based on the dual Voronoi diagram; and 5) Take the Voronoi edges as the elements of the flow lattice.

In the dual-lattice models, fracture analyses are performed on the structural lattice, whereas flow analyses are performed on the flow lattice. A potential cracking surface is the shared facet of two adjacent Voronoi cells as seen in **Figure 2**. It is noted that this surface coincides with a flow lattice element in two dimensions and is bounded by flow lattice elements in three dimensions. To couple the fracture and flow analyses, the amount of crack opening is evaluated for each structural element exhibiting fracture. The crack opening associated with a structural lattice element can be related to an increase of the permeability of the surrounding flow lattice elements, in accordance with theory or experimental observations [9-11].

2.2 Fracture analyses

Each point used in the Delaunay tessellation has three degrees of freedom in two dimensions and six in three dimensions. Normal, shear, and rotational springs are placed between two Voronoi cells as shown in **Figure 2**.

Concrete materials are assumed to crack when the stress reaches the prescribed tensile strength, and to soften according to a prescribed stress-crack opening relation (**Figure 3**).

Additional details and validations of fracture analyses on the structural lattice have been presented elsewhere [1-4]. This paper focuses on the development of the flow lattice for flow analyses, with emphasis on the effects of cracking.

2.3 Flow analyses

The governing equation for the flow analyses appears as either the diffusion equation or the advection equation in the literature [12,13]. Transport of heat, moisture, oxygen, or carbon dioxide is expressed as a diffusion phenomenon, whereas ionic transport such as that of chloride or other ions is partly regarded as an advection phenomenon.

In the present study, the following advection-diffusion equation is assumed to govern.

$$\frac{\partial \theta}{\partial t} - \nabla \cdot \left(D \nabla \theta \right) + \nabla \cdot \left(\theta \boldsymbol{u} \right) = 0 , \tag{1}$$

where θ is the unknown scalar function, t is time, D is the diffusion coefficient, and $\boldsymbol{u}$ is a given velocity. No internal source or sink term is considered in **Eq. (1).**

The authors have discretized Eq. (1) using the finite volume method [7] as done on the structural lattice in the literature [14,15]. The derived semi-discrete equations are:

$$\boldsymbol{M}\dot{\boldsymbol{\theta}} + \boldsymbol{K}\boldsymbol{\theta} + \boldsymbol{B}\boldsymbol{\theta} = \boldsymbol{f} , \tag{2}$$

$$\boldsymbol{M} = \mathop{\mathrm{A}}_{e} \boldsymbol{M}_e ; \; \boldsymbol{M}_e = \frac{A_e h_e}{6d} \begin{pmatrix} 2 & 1 \\ 1 & 2 \end{pmatrix}, \tag{3a, 3b}$$

$$\boldsymbol{K} = \mathop{\mathrm{A}}_{e} \boldsymbol{K}_e ; \; \boldsymbol{K}_e = \frac{D_e A_e}{h_e} \begin{pmatrix} 1 & -1 \\ -1 & 1 \end{pmatrix}, \tag{4a, 4b}$$

$$\boldsymbol{B} = \mathop{\mathrm{A}}_{e} \boldsymbol{B}_e ; \; \boldsymbol{B}_e = \frac{A_e \boldsymbol{u} \cdot \boldsymbol{n}_e}{2} \begin{pmatrix} 1 & 1 \\ -1 & -1 \end{pmatrix}, \tag{5a, 5b}$$

where $\mathop{\mathrm{A}}_{e}$ denotes the assembling procedure, $\boldsymbol{\theta}$ is the column vector of the unknown scalar

values at all the nodes including those with Dirichlet boundary conditions, $\dot{\boldsymbol{\theta}}$ is the time derivative of $\boldsymbol{\theta}$, $\boldsymbol{M}$ is the total capacity matrix, $\boldsymbol{K}$ is the total diffusivity matrix, $\boldsymbol{B}$ is the total advection matrix, $\boldsymbol{f}$ is the term due to the Neumann boundary conditions, $\boldsymbol{M}_e$, $\boldsymbol{K}_e$, and $\boldsymbol{B}_e$ are the elemental capacity, diffusivity, and advection matrices, respectively, d equals 2 in two dimensions and 3 in three dimensions, A_e and h_e are the facet area and the length of element e, respectively (see **Figures 4 and 5**), and $\boldsymbol{n}_e$ is the unit normal to the facet from node i to node j. It should be noted that these elemental matrices coincide with those obtained by the finite volume method on the structural lattice [16,17].

The semi-discrete equation, **Eq. (2)**, is discretized in time and solved using the Crank-Nicolson scheme [18].

3 VERIFICATIONS

3.1 Linear transient diffusion in a three-dimensional random lattice

A linear transient diffusion problem on a cubic domain is solved as a verification of the three-dimensional random lattice (**Figure 6**). The initial conditions and boundary conditions are expressed by **Eqs. (6) and (7)**, respectively. Zero flux conditions are imposed on the other boundary surfaces.

$$\theta(x,y,z,t=0)=\sin\frac{\pi x}{L}. \tag{6}$$

$$\theta(x=0,y,z,t)=\theta(x=L,y,z,t)=0. \tag{7}$$

The initial condition and the potential development in time appear as blue dots in **Figure 6** (right), together with the analytical solutions of **Eq. (8)** drawn in red lines.

$$\theta(x,y,z,t)=\exp\left(-\frac{\pi^2 t}{L^2}\right)\sin\frac{\pi x}{L}. \tag{8}$$

The lattice solutions precisely agree with the analytical solutions. It is verified that the three-dimensional random lattice, constructed on the edges of the Voronoi polyhedra, solves linear transient diffusion problems.

3.2 Periodic advection flow in a plane

An advection problem on a square domain of L by L is considered to demonstrate the capability of solving the advection equation. The sine distribution of **Eq. (9)** serves as the initial condition, and the periodic boundary condition of **Eq. (10)** is provided. The domain is quasi-regularly discretized as presented in **Figure 7** (a).

$$\theta(x,y,t=0)=\sin\frac{2\pi x}{L}. \tag{9}$$

$$\theta(x+L,y,t)=\theta(x,y+L,t)=\theta(x,y,t). \tag{10}$$

The evolution of the potential distribution in time is shown in **Figure 7** (b). The periodicity is well reproduced despite some dispersion. Thus, it is verified that the advection equation can be solved on the two-dimensional flow lattice.

3.3 Water absorption in uncracked concrete

Water absorption in uncracked concrete is simulated to verify the capability of solving non-linear diffusion problems. The Darcian-flow modeling of capillary suction through concrete, expressed in terms of hydraulic diffusivity [19], is adapted in this study. The diffusion coefficient of such flow is given as **Eq. (11)**, which is defined as an exponential function of reduced water content.

$$D(\theta)=D_0\exp n\theta, \tag{11}$$

$$\theta=\frac{\Theta-\Theta_r}{\Theta_s-\Theta_r}, \tag{12}$$

where θ is the potential variable representing the reduced water content, also known as the normalized water content or effective saturation, i.e. θ ranges from 0 to 1, D_0 is the base diffusion coefficient at θ=0, n is the shape term governing the profile shape, Θ is the volumetric water content, Θ_r is the residual water content, and Θ_s is the saturated water content. D_0=2.2×10^{-4} (mm^2/s) and n=6.4 [20] are used in the following simulation. It is noted that capillary suction models for unsaturated soil can be used as alternative formulations on the dual lattice [21].

The domain, the discretization, and the boundary conditions are shown in **Figure 8** (a). The domain is a square of 30 mm by 30 mm in two dimensions. Zero-flux (q_n=0) boundary conditions are imposed on the three edges, whereas the θ= 1 potential boundary condition is imposed on the other edge. The initial condition is θ=0 all over the domain.

The calculated distributions of the reduced water content at t=3, 15, and 60 min are shown in **Figure 8** (b). It is observed that water ingresses from the bottom with some degree of uniformity. The solution along y axis (indicated as "lattice") is compared with the one-dimensional finite difference solutions (indicated as "FDM") in **Figure 8** (c). The lattice solutions exhibit a slight delay from the finite difference solutions. The oscillation observed at t=3 min disappears at t=60 min.

To quantitatively investigate the precision of the lattice solutions, we have calculated the sorptivity s as defined in **Eq. (13)** [20].

$$s = \int_0^1 \lambda \, \mathrm{d}\theta , \tag{13}$$

$$\lambda = x t^{-1/2} , \tag{14}$$

where λ is the Boltzmann variable, x is the location variable (indicated as y in **Figure 8** (c)), and t is time. Since **Eq. (13)** is of one dimension, and the lattice models are of higher dimensions, we cannot directly evaluate **Eq. (13)** with the dual-lattice models. Therefore, the sorptivity of the lattice solution is calculated with **Eq. (15)**, in which the polygonal Voronoi cells are divided into a set of triangles Ω_j and the potential distribution θ is integrated over these triangles using Gaussian quadrature [22], followed by division by the dimension of x and the square root of time t.

$$s = \frac{1}{L\sqrt{t}} \sum_j \int_{\Omega_j} \theta(t) \, \mathrm{d}\Omega_j . \tag{15}$$

This sorptivity is compared with an approximation, which is suggested by Parlange et al. [23] in **Eq. (16)**, as listed in **Table 1**. These two values show good agreement within 2% difference. Hence, it has been shown that the dual lattice solves non-linear diffusion problems with good accuracy.

$$\frac{s^2}{D_0} \approx e^n \left(2n^{-1} - n^{-2}\right) - n^{-1} - n^{-2} . \tag{16}$$

Table 1: Comparison of sorptivity values

Method	Sorptivity (mm s$^{-1/2}$)
Lattice solution (at t=60 min)	0.191
Approx. solution by **Eq. (16)**	0.195

4 NUMERICAL SIMULATIONS

4.1 Target experiment

The water absorption experiments performed by Zhang et al. [24] are simulated by the dual-lattice models. In this experiment, some sections of steel reinforced concrete, the dimensions of which are 100 mm × 100 mm × 25 mm, were prepared. The sections were equipped with two steel bars of 8-mm diameter, located in the lower and upper portions of the section, respectively. Each specimen has a single flexural crack of approximately 0.35 mm width at the center, which was introduced through a three-point bending loading. The bottom face of each specimen was soaked in water, with the sides being covered by aluminum foil after complete drying over a four-day period. The progress of water absorption was observed through the neutron radiography technology, and given as grey-scale images.

4.2 Numerical models

The Voronoi diagram used in the simulation is drawn in **Figure 9**. The locations of the vertical flexural crack and two horizontal debonded zones are also indicated in the figure as well as the boundary conditions. The initial condition θ=0 is imposed through the domain.

Based on the verification exercise presented in section 3.3, seven sets of base diffusion coefficients are simulated as listed in **Table 2**. The lattice elements represent one of four

features: matrix, flexural crack, and lower and upper debonded zones. The diffusion coefficients of each feature are different, such that they represent the effects of crack opening and fracture damage on permeability. These parameters are determined so as to reproduce the experimental observations. The shape term in the diffusion coefficient of **Eq. (11)** is fixed to be n=6.4 as suggested by Leech et al. [20]. Case B is the base set of diffusion coefficients, from which comparisons can be made. For example, cases A, B, and C elucidate the role of the matrix diffusion coefficient; cases B, D, and E clarify the influence of the flexural crack diffusion coefficient; and cases B, F, and G permit study of the diffusion coefficient of the debonded zones.

Table 2: Base diffusion coefficient D_0 (mm^2/s)

case	matrix	flexural crack	debonded (lower)	debonded (upper)
A	2.4×10^{-4}	2.4×10^{-1}	0.6×10^{-2}	0.3×10^{-2}
B	1.2×10^{-4}			
C	0.6×10^{-4}			
D	1.2×10^{-4}	7.2×10^{-1}		
E		0.8×10^{-1}		
F		2.4×10^{-1}	1.8×10^{-2}	0.9×10^{-2}
G			0.2×10^{-2}	0.1×10^{-2}

4.3 Numerical results

The left column of **Figure 10** is the ratio of absorbed water content to the total absorbable water content at location y, which is calculated as

$$\bar{\theta}(y,t) = \frac{1}{L}\int_{-L/2}^{L/2} \theta(x,y,t)\,\mathrm{d}x\,. \qquad (17)$$

For t=1, 5, and 30 min, the results of cases B, D, and E are displayed to compare the effect of the diffusion coefficient for the flexural crack. Larger diffusion coefficients provide higher water content distributions, i.e. case D shows the highest water content distributions, and the case E shows the lowest. Case B shows good agreement with experimental results at earlier times (t=1 to 30 min).

For t=60, 120, and 480 min, cases B, F, and G compare the effect of the debonded zone diffusion coefficients. The qualitative observation is similar to that for the previous cases, t=1, 5, and 30 min, i.e. larger diffusion coefficients provide higher water content distributions. For these results, case B shows higher water content distributions compared to the experimental results.

The middle-right column of **Figure 10** presents contour images of the reduced water content distributions for case B, whereas the middle-left column presents grey-scale images of water content measured by Zhang et al. using neutron radiography [24]. Water first penetrates the flexural crack, and then progresses into the debonded zones. As the flexural crack and debonded zones become saturated, water gradually ingresses into matrix. Along with water entering from the bottom face, the specimen becomes nearly saturated at t=480 min. The contour image at 480 min resembles that obtained through the experiment, in particular with respect to the low water content regions at the middle of both sides.

The right column of **Figure 10** is the reduced water content at the middle of the sections at y=50mm. For t=1, 5, and 30 min, cases B, D, and E show the influence of the flexural crack diffusion coefficients. Cases B and D show better results than that of case E, although these three cases show almost no difference for these times. For t=60, 120, and 480 min, cases A, B, and C are chosen to study the effect of matrix diffusion coefficient. In all cases, it is observed that the flexural crack first becomes saturated, and then water ingresses into the matrix. Case A reaches the almost saturated state too early. Cases B and C exhibit better results, similar to those of the experiments.

4.4 Discussions

Differences between the lattice model and experimental results may be due to several reasons. While the neutron radiography detects the absolute water content, the current method calculates the reduced water content, i.e. the ratio of absorbed water content to the total

absorbable water content. In the proposed model, the volume of steel reinforcing bars is treated as that of normal concrete. Hence, the volume of steel reinforcing bars should be subtracted from the numerical results if directly compared with experimental results. This would be achieved by three-dimensional analyses with the volume of the steel reinforcing bars explicitly modeled.

The contour images of **Figure 10** (middle) provide slightly different results from those obtained through experiments. The difference comes, in part, from the assumption that the base diffusion coefficient of each region is constant. It is likely that flexural loading produces non-uniform distribution of stresses and strains along the vertical axis. This leads to the non-uniform crack opening along the crack path and also non-uniform debonding of the steel reinforcement bars. Thus, it is expected that graded diffusion coefficients along the flexural crack and debonded zones should produce more realistic results.

5 CONCLUSIONS

This paper has reviewed fundamental concepts of a dual-lattice model, which is based on the duality between the Delaunay tessellation and Voronoi diagram generated from a random set of points. The discrete advection-diffusion equation on the flow lattice has been described with reference to the finite volume method. This proposed method has been verified by solving a linear transient diffusion problem, a linear advection problem, and a non-linear diffusion problem. The solutions obtained via the dual lattice have shown good agreement with analytical or other numerical solutions.

Finally, numerical simulations of water absorption in cracked reinforced concrete have demonstrated the capabilities of the present method through qualitative comparisons with those obtained by the neutron radiography experiments. The simulated results suggest that closer agreement with the experimental results could be obtained with more realistic settings of the diffusion coefficients. In future work, the proposed method could be extended to simulate more complicated durability problems of reinforced concrete structures such as those due to the ingress of chlorides and sulfates, carbonation, or steel corrosion.

REFERENCES

[1] Schlangen, E. and Van Mier, J.G.M., 1992. Simple lattice model for numerical simulation of fracture of concrete materials. *Materials and Structures*, **25**:534-542.

[2] Bolander, J.E. and Saito, S., 1998. Fracture analyses using spring networks with random geometry. *Engineering Fracture Mechanics*, **61**:569-591.

[3] Berton, S. and Bolander, J.E., 2006. Crack band model of fracture in irregular lattices. *Compt. Methods Appl. Mech. Engrg.*, **195**:7172-7181.

[4] Cusatis, G., Pelessone, D., and Mencarelli, A., 2011. Lattice discrete particle model (LDPM) for failure behavior of concrete. I: Theory. *Cement and Concrete Composites*, **33** (9):881-890.

[5] Grassl, P., 2009. A lattice approach to model flow in cracked concrete. *Cement and Concrete Composites*, **31**:454-460.

[6] Grassl, P. and Bolander, J.E., 2009. Three-dimensional lattice model for coupling of fracture and flow. In D.R.J. Owen and E. Oñate (eds), *International Conference on Particle-Based Methods*, November 25-27, 2009, Barcelona, Spain; pp.154-157.

[7] Saka, T., Bolander, J.E. and Grassl, P., 2012. Dual-lattice models of coupled fracture-flow in quasi-brittle materials. In Japan Society of Computational Engineering and Science (JSCES), *17th Japan Computational Engineering Conference*, May 29-31, 2012, Kyoto, Japan; paper no. A-9-5 on CD-ROM.

[8] Taniguchi, T. and Moriwaki, K., 2006. *Automatic element generation for the three-dimensional finite element method*. Morikita Shuppan, Japan. ISBN: 4-627-91891-7. (in Japanese; Title has been translated by the author of this paper.)

[9] Witherspoon, P.A., Wang, J.S.Y., Iwai, K., and Gale, J.E., 1980. Validity of cubic law for fluid flow in a deformable rock fracture. *Water Resources Research*, **16**:1016-1024.

[10] Wang, K., Jansen, D.C., and Shah, S.P., 1997. Permeability study of cracked concrete. *Cement and Concrete Research*, **27** (3):381-393.

[11] Aldea, C-M., Ghandehari, M., Shah, S.P., and Karr, A., 2000. Estimation of water flow through cracked concrete under load. *ACI Material Journal*, **97**:567-575.

[12] Samson, E., Marchand, J., Snyder, K.A., and Beaudoin, J.J., 2005. Modeling ion and fluid transport in unsaturated cement systems in isothermal conditions. *Cement and Concrete Research*, **35**:141-153.

[13] Samson, E. and Marchand, J., 2007. Modeling the effect of temperature on ionic transport in cementitious materials. *Cement and Concrete Research*, **37**:455-468.

[14] Sukumar, N., 2003. Voronoi cell finite difference method for the diffusion operator on arbitrary unstructured grids. *Int. J. Numer. Meth. Engrg*, **57**:1-34.

[15] Hüttig, C. and Stemmer, K., 2008. Finite volume discretization for dynamic viscosities on Voronoi grids. *Physics of the Earth and Planetary Interiors*, **171**:137-146.

[16] Apanovich, Y.V. and Lyumkis, E.D., 1988. Difference schemes for the Navier-Stokes equations on a net consisting of Dirichlet cells. *USSR Computational Mathematics and Mathematical Physics*, **28** (2):57-63.

[17] Taniguchi, N. and Kobayashi, T., 1991. Finite volume method on the unstructured grid system, *Computers & Fluids*, **19** (3/4):287-295.

[18] Crank, J. and Nicolson, P., 1947. A practical method for numerical evaluation of solutions of partial differential equations of the heat-conduction type. *Proc. Camb. Phil. Soc.*, **43**:50-67.

[19] Hall, C., 1989. Water sorptivity of mortars and concretes: a review. *Magazine of Concrete Research*, **41**:51-61.

[20] Leech, C., Lockington, D., and Dux, P., 2003. Unsaturated diffusivity functions for concrete derived from NMR images. *Materials and Structures*, **36**:413-418.

[21] Grassl, P., Fahy, C., Gallipoli, D., and Bolander, J.E., 2012. A lattice model for fracture and mass transport in concrete. In *2nd International Conference on Microstructure Related Durability of Cementitious Composites*, April 11-13, 2012, Amsterdam, The Netherlands.

[22] Cowper, G.R., 1973. Gaussian quadrature formulas for triangles. *Int. J. Numer. Meth. Engrg*, **7** (3):405-408.

[23] Parlange, M.B., Prasad, S.N., Parlange, J.-Y., and Romkens, M.J., 1992. Extension of the Heaslet-Alksne technique to arbitrary soil water diffusivities. *Water Resources Research*, **28** (10):2793-2797.

[24] Zhang, P., Wittmann, F.H., Zhao, T. and Lehmann, E.H., 2010. Neutron imaging of water penetration into cracked steel reinforced concrete. *Physica B*, **405**:1866-1871.

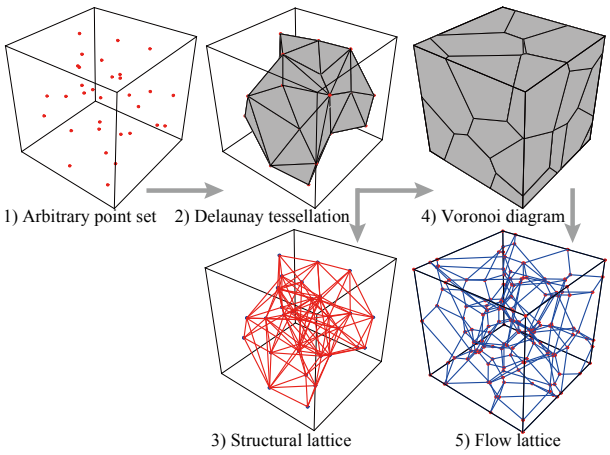

Figure 1: Generation procedure of dual-lattice models.

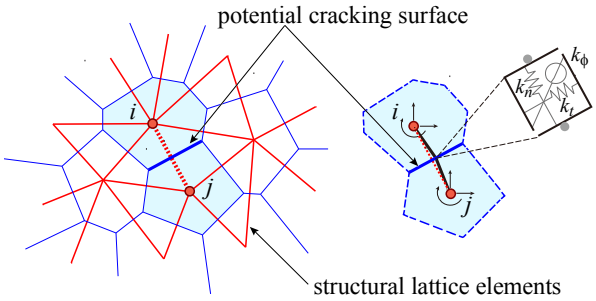

Figure 2: Configuration of structural lattice elements in two dimensions (left) and normal and shear springs of a structural lattice element (right).

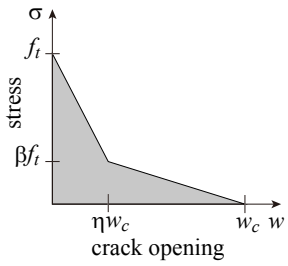

Figure 3: Typical stress versus crack opening relation [3].

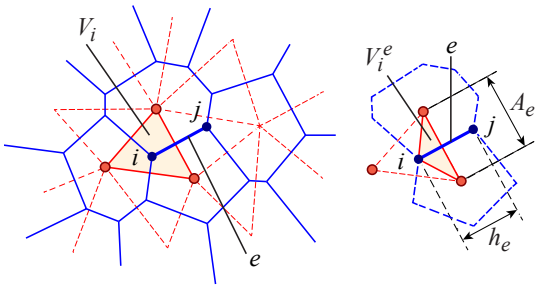

Figure 4: Configuration of flow lattice elements in two dimensions (left) and elemental dimensions of a flow element (right).

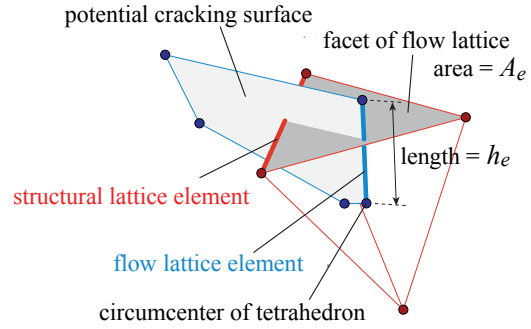

Figure 5: Configuration and elemental dimensions of dual-lattice elements in three dimensions.

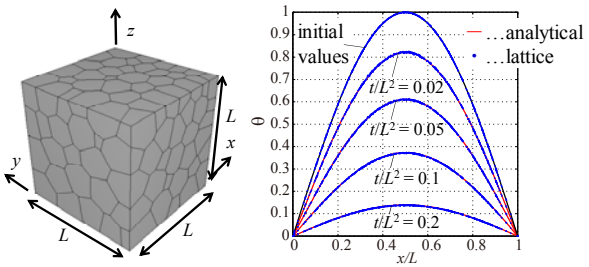

Figure 6: Linear transient diffusion in three dimensions: (left) Irregular discretization of domain; and (right) computed results with analytical solutions.

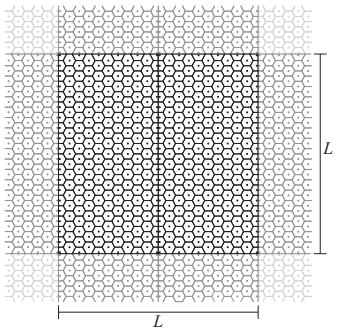

(a) Discretization of domain with periodic boundary conditions.

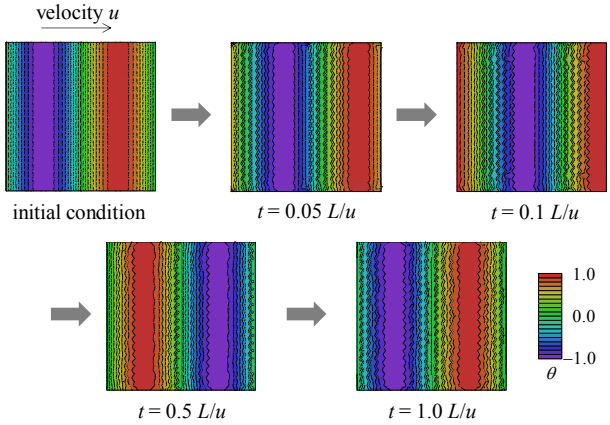

(b) Initial condition (upper left) and computed solutions.

Figure 7: Linear advection in infinite plane.

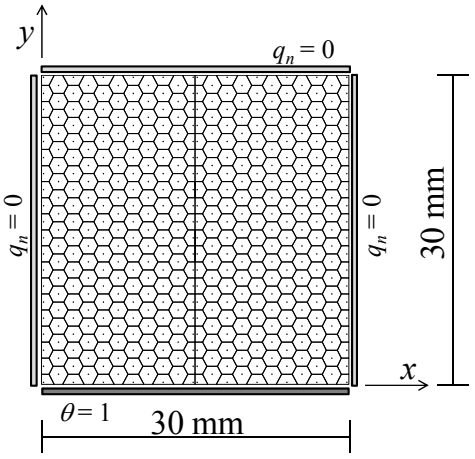

(a) Discretization of target domain and boundary conditions.

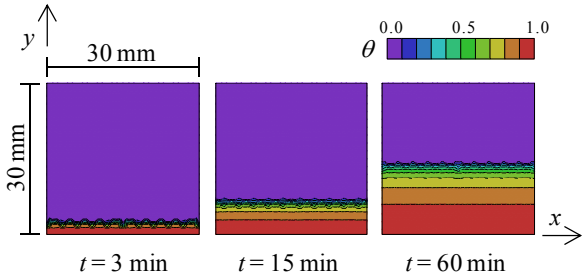

(b) Computed reduced-water-content distributions.

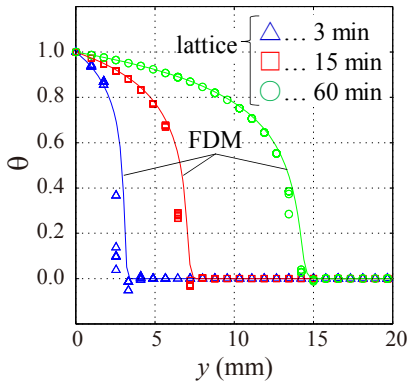

(c) Computed reduced water content distributions along y axis (indicated as "lattice"), compared with finite difference solutions (indicated as "FDM").

Figure 8: Water absorption in uncracked concrete.

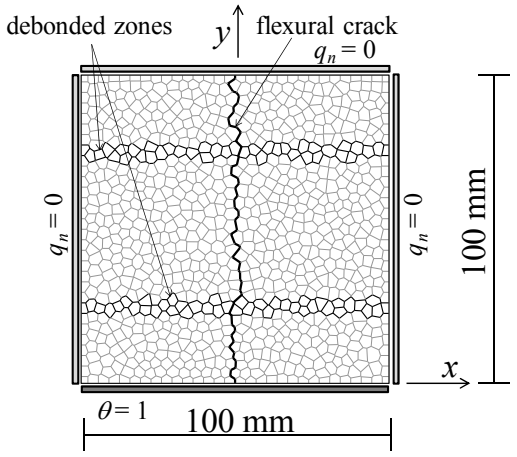

Figure 9: Water absorption in cracked reinforced concrete: Voronoi diagram of domain, locations of flexural crack and debonded zones, and boundary conditions.

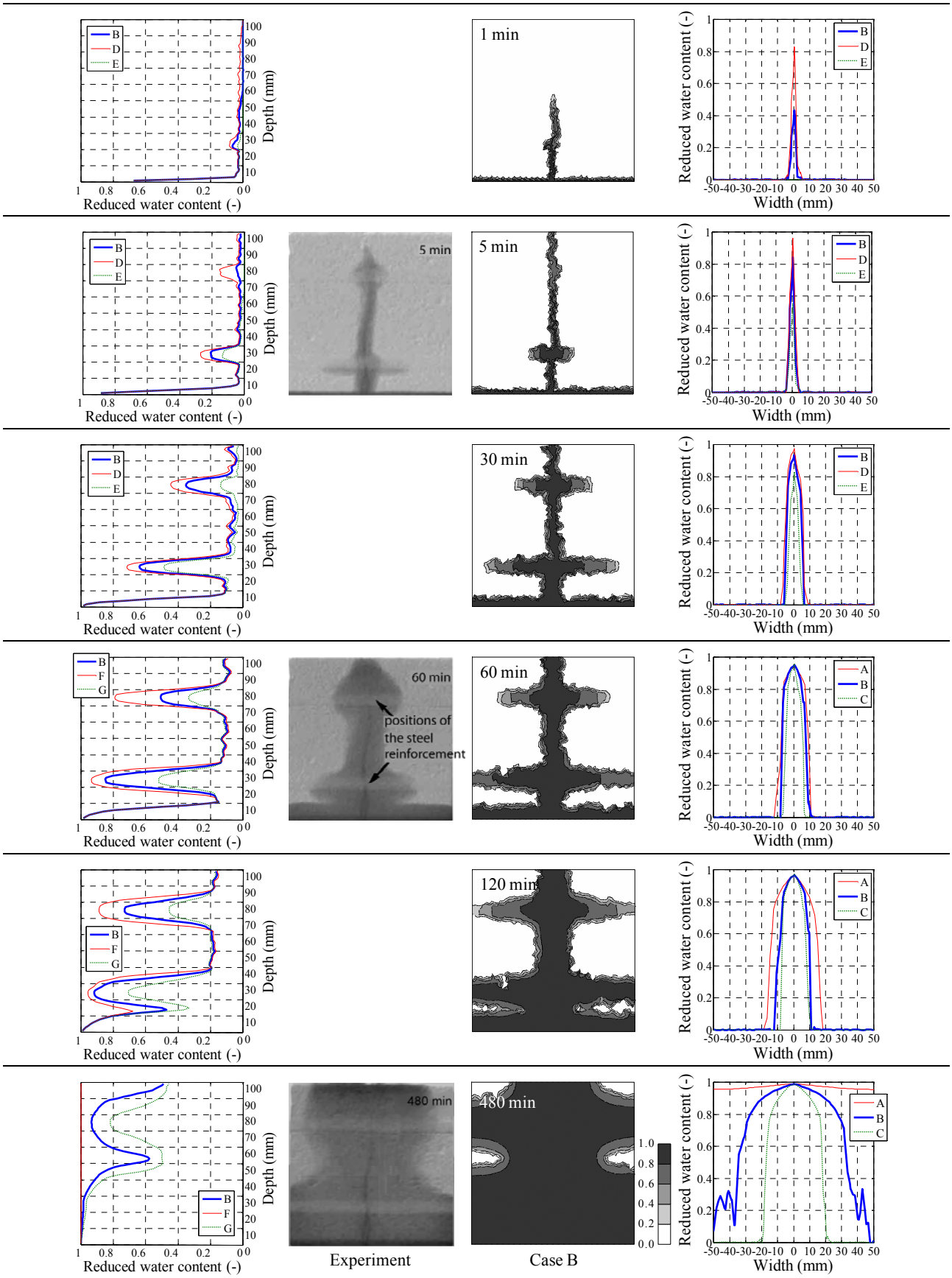

Figure 10: Reduced-water-content distributions in cracked reinforced concrete: (left) calculated via **Eq. (17)** along vertical axis; (middle-left) images of water penetration obtained via neutron radiography (adapted from [24]); (middle-right) of case B in contour images; and (right) along horizontal axis at mid-height.